Meteoritics & Planetary Science 37, 1599–1614 (2002)
Available online at http://www.uark.edu/meteor

Low-energy helium ion irradiation-induced amorphization and chemical changes in olivine: Insights for silicate dust evolution in the interstellar medium

PHILIPPE CARREZ[1], KARINE DEMYK[2,3], PATRICK CORDIER[1], LÉON GENGEMBRE[4], JEAN GRIMBLOT[4], LOUIS D'HENDECOURT[2], ANTHONY P. JONES[2] AND HUGUES LEROUX[1]*

[1]Laboratoire de Structure et Propriétés de l'Etat Solide (ESA CNRS 8008), Bât. C6, Université des Sciences et Technologies de Lille, 59655 Villeneuve d'Ascq Cedex, France
[2]Institut d'Astrophysique Spatiale, IAS-CNRS, "Astrochimie Expérimentale", Université Paris XI, 91405 Orsay Cedex, France
[3]FOM Institute for Plasma Physics Rijnhuizen, Postbox 1207, 3430 BE Nieuwegein, The Netherlands
[4]Laboratoire de Catalyse de Lille (ESA CNRS 8010), Bât. C3, Université des Sciences et Technologies de Lille, 59655 Villeneuve d'Ascq Cedex, France
Correspondence author's e-mail address: hugues.leroux@univ-lille1.fr

(Received 2002 March 5; accepted in revised form 2002 August 5)
(Presented at "Laboratory Simulations of Circumstellar Dust Analogs: Expectations for Comet Nucleus Encounters", a special session of the 64th annual Meteoritical Society meeting, Vatican City, 2001 September 13)

Abstract–We present the results of irradiation experiments aimed at understanding the structural and chemical evolution of silicate grains in the interstellar medium. A series of He^+ irradiation experiments have been performed on ultra-thin olivine, $(Mg,Fe)_2SiO_4$, samples having a high surface/volume (S/V) ratio, comparable to the expected S/V ratio of interstellar dust. The energies and fluences of the helium ions used in this study have been chosen to simulate the irradiation of interstellar dust grains in supernovae shock waves. The samples were mainly studied using analytical transmission electron microscopy. Our results show that olivine is amorphized by low-energy ion irradiation. Changes in composition are also observed. In particular, irradiation leads to a decrease of the atomic ratios O/Si and Mg/Si as determined by x-ray photoelectron spectroscopy and by x-ray energy dispersive spectroscopy. This chemical evolution is due to the differential sputtering of atoms near the surfaces. We also observe a reduction process resulting in the formation of metallic iron. The use of very thin samples emphasizes the role of surface/volume ratio and thus the importance of the particle size in the irradiation-induced effects. These results allow us to account qualitatively for the observed properties of interstellar grains in different environments, that is, at different stages of their evolution: chemical and structural evolution in the interstellar medium, from olivine to pyroxene-type and from crystalline to amorphous silicates, porosity of cometary grains as well as the formation of metallic inclusions in silicates.

INTRODUCTION

The study of silicate dust in various astrophysical environments has recently gone through a renewal of interest with the extensive spectroscopic results provided by the infrared space observatory (ISO) (Kessler *et al.*, 1996). The ISO spectroscopic results have shown the presence of crystalline silicate dust grains in evolved star outflows (Waters *et al.*, 1996), in young star environments (Malfait *et al.*, 1998; Waelkens *et al.*, 1996, 1998) as well as in some comets (Crovisier *et al.*, 1997). In contrast, crystalline silicate signatures are absent in the interstellar medium: diffuse interstellar medium and molecular clouds around some protostars are characterized by the presence of fully amorphous silicate dust (Demyk, 2000; Li and Draine, 2001). Since interstellar silicates originate mainly from evolved star outflows, the absence of crystalline signature shows that the dust undergoes a strong structural modification in the interstellar medium during its lifetime, between its formation in the envelopes of late-type stars, and its incorporation into the regions around young stars and their associated protoplanetary accretion disks.

Although the medium is very cold, the dust in the interstellar medium is subjected to a wide variety of processes that can modify its structure, for example, grain–grain collisions, irradiation by cosmic rays or by light ions accelerated by shock waves originating from supernovae (*e.g.*, Jones *et al.*, 1996). A review of the evolution of interstellar dust was recently presented by Jones (2000). Thanks to the ISO results, extensive new data are now available for furthering our understanding of dust evolution and the physical processes that can act on it.

Prelude preprint MS#4785
© Meteoritical Society, 2002. Printed in USA.

In recent years, the ISO spectra of the amorphous and crystalline silicate signatures have been tested against the results of laboratory and theoretical studies of annealing (*e.g.*, Brucato *et al.*, 1999; Fabian *et al.*, 2000; Hallenbeck *et al.*, 1998) and irradiation experiments (*e.g.*, Demyk *et al.*, 2001; Carrez *et al.*, 2002). From these joint approaches, significant advances in our understanding of the origin and evolution of interstellar silicates can be expected. Among these studies the physics of the crystalline–amorphous transition in silicates is one of the key points for study.

This study is the second contribution in an experimental research program on silicate dust evolution under the effects of irradiation. In our first contribution (Demyk *et al.*, 2001), we have shown that the irradiation of dust in supernovae shock waves can significantly alter the structural signature of the silicates. The present study is a direct continuation of this approach and includes additional results for He^+ ion implantation into olivine by extending the energy range and the fluence of the incident helium ions. The crystalline–amorphous transition under ion irradiation has been investigated in detail and the important role of the surfaces has been considered. We also focus on studying the associated chemical changes using analytical transmission electron microscopy (ATEM) and x-ray photoelectron spectroscopy (XPS).

EXPERIMENTAL PROCEDURE

Sample Preparation

The samples selected in this study are terrestrial olivine single crystals from San Carlos (Arizona), with $Mg_{1.8}Fe_{0.2}SiO_4$ composition. To reproduce the behaviour of small interstellar silicate particles the samples must exhibit high surface/volume ratio. Their geometry must also be adapted for a subsequent microstructural characterization. These requirements are met with ultra-thin transmission electron microscope (TEM) specimens. Sample preparation first involves making doubly-polished 30 μm thick specimen. The samples are then glued on standard, 3 mm TEM Cu grids, and ion thinned with a low (15°) beam angle with Ar^+ ions accelerated at 5 kV. Ion thinning is stopped when a small hole is formed in the middle of the sample. The rim of the hole gives a bevel-edged region with a thickness decreasing to zero (Fig. 1). The edge of the sample exhibits a very high surface/volume ratio, comparable to that expected from a "classical" silicate dust grain in the interstellar medium, and is transparent to electrons of a TEM allowing microstructural investigations.

Helium Ion Irradiation

The He^+ irradiation was performed on the ultra-thin TEM samples (Fig. 1) at the Centre de Spectrométrie Nucléaire et de Spectrométrie de Masse (CSNSM, Orsay, France) at room temperature under vacuum at a residual pressure of 10^{-7} mbar. The beam current density was maintained below 9 $\mu A/cm^2$ and the ion beam (section of 5 mm^2) was scanned homogeneously over the samples in order to prevent heating during irradiation. He^+ ions were accelerated at 4, 10 and 50 keV with fluences in the range 5×10^{15} to 10^{18} ions/cm^2. The experimental conditions are summarised in Table 1.

Transmission Electron Microscope Characterization

After irradiation the samples were investigated by different TEM techniques (selected area electron diffraction (SAED), bright- and dark-field imaging, x-ray microanalysis). Thus, they were coated with a carbon layer (about 10–20 nm thick) to prevent charging effects under the electron beam. The TEM

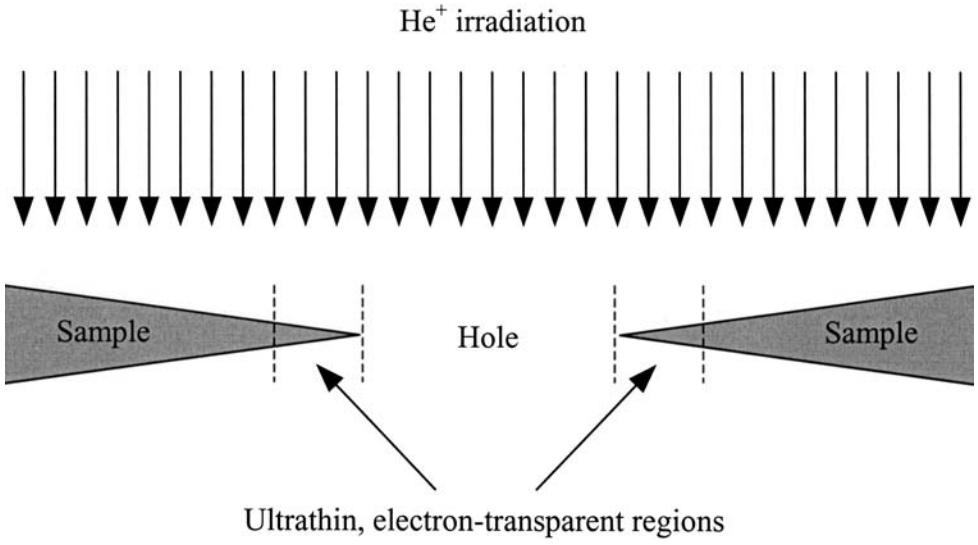


FIG. 1. Experimental configuration of He^+ irradiation. Due to TEM specimen preparation, the sample is bevel-shaped with a hole in the middle.

TABLE 1. Summary of irradiation experiments.*

Sample number	Sample type	Irradiation conditions	
		Energy (keV)	Fluence (ion/cm^2)
0	Ultra-thin	Not irradiated	–
1	Ultra-thin	4	5×10^{15}
2	Ultra-thin	4	10^{16}
3	Ultra-thin	4	5×10^{16}
4	Ultra-thin	4	10^{17}
5	Ultra-thin	4	5×10^{17}
6	Ultra-thin	4	10^{18}
7	Bulk	4	10^{17}
8	Ultra-thin	10	10^{18}
9	Ultra-thin	50	10^{18}

*Ultra-thin samples are designed for TEM observations. The bulk specimen (experiment #7) was characterized by XPS.

investigations were performed with a Philips CM 30 operating at 300 kV. The microscope is equipped with an x-ray energy-dispersive spectrometer (EDS; Noran-Voyager) with a Ge detector and an ultra-thin window, which allows low-energy characteristic x-ray lines such as O_K line (523 eV) to be detected with a good sensitivity. The detector sensitivity factors (k-factors) which depends on the characteristics of the EDS system, were determined by the "parameter less extrapolation method" proposed by Van Cappellen (1990). Quantitative microanalysis requires a precise thickness determination to be performed. We used the absorption correction method developed by Van Cappellen and Doukhan (1994) for stoichiometric oxide compounds. By this method, the thickness is deduced from spectra by comparing the intensity of O with those of the different cations. Practically, thickness parameter is adjusted until electroneutrality of the compounds is reached in the quantification program. This requires a detector having a good sensitivity to oxygen. A precise description of the $k_{X/Si}$ factor determination and of k_{abs} measurements is given in Carrez *et al.* (2001).

X-ray microanalyses were performed using the scanning (STEM) mode with a low current density in order to minimise possible electron irradiation damages occurring under the beam. The evolution of the material under the electron beam was monitored by chronospectroscopy. Three consecutive EDS spectra were recorded at each point to follow the evolution of the apparent composition with acquisition time. The true composition was obtained by extrapolation at zero electron-irradiation time. In general, this additional correction is low.

X-Ray Photoemission Spectroscopy

The chemical analysis of the bulk olivine samples were performed by XPS which provides information from below (30–50 Å) the surface, before and after He^+ irradiation. The experiments were performed using the ESCALAB 220XL spectrometer from Thermo VG Scientific. The non-monochromatised aluminium source ($Al_{K\alpha}$ = 1486.6 eV) was used for excitation with a 300 W applied power. Analyses were operated with a constant pass energy (CAE; E = 40 eV), using the electrostatic mode for the lens. Photoelectrons were collected from a 5 mm diameter area by reducing the field of view and angle acceptance apertures. The data were processed by means of the Eclipse Software (from VG Scientific) after a Shirley-type baseline removal (Shirley, 1972).

Atomic ratios of the outer layers were calculated from the normalised area:

$$\text{Normalized area} = \text{peak area} / [T(E) \times \Lambda(E) \times \sigma]$$

With, σ cross-section of the core level (Scofield, 1976), T(E) transmission function of the spectrometer and Λ(E) inelastic mean free path of electron in inorganic compounds ~$kE^{0.77}$ (Wagner *et al.*, 1980; Tamuna *et al.*, 1993).

The binding energy scale was initially calibrated against the $Au_{4f7/2}$ (84 eV), $Cu_{2p3/2}$ (932.7 eV) and $Ag_{3d5/2}$ (368.3 eV) levels. The Mg $KL_{23}L_{23}$ Auger peak (1180.4 eV kinetic energy) was used as internal reference in case of large charging effect.

For XPS experiments, He^+ irradiation was performed in the preparation chamber attached to the analysis chamber of the spectrometer. The AG5000 cold cathode ion gun (VG Scientific) was operated at 4 keV. Helium pressure was kept ~8×10^{-6} mbar. The measured sample current was 50 μA for a beam diameter of 6 mm.

INVESTIGATION OF THE IRRADIATED SAMPLES

Microstructural Evolution

The TEM micrograph of the non-irradiated sample is characterized by the typical contrast of a perfect crystal with Bragg contours (which appear dark in bright-field) corresponding to the locus of the exact Bragg conditions. Samples #1 and #2 irradiated at 4 keV with fluences of 5×10^{15} and 10^{16} ions/cm^2, respectively, present these Bragg contours and are thus similar to the reference sample, even if they present tiny bubbles or voids making the surface appearing like an "orange skin". Samples irradiated at higher fluences (*i.e.*, 5×10^{16} ions/cm^2 and above: samples #3 to #6) exhibit several characteristic features (Fig. 2). The most prominent feature is the rim that appears in the thinnest part of the specimen. This rim is easily recognised because it contains no Bragg contours, whatever the orientation of the sample, suggesting an amorphous structure. This is confirmed by SAED performed on the rim and which shows the typical diffuse rings of amorphous materials. Microanalysis shows that the rim is close to olivine composition. SAED performed on crystalline regions (which display Bragg contours, in black

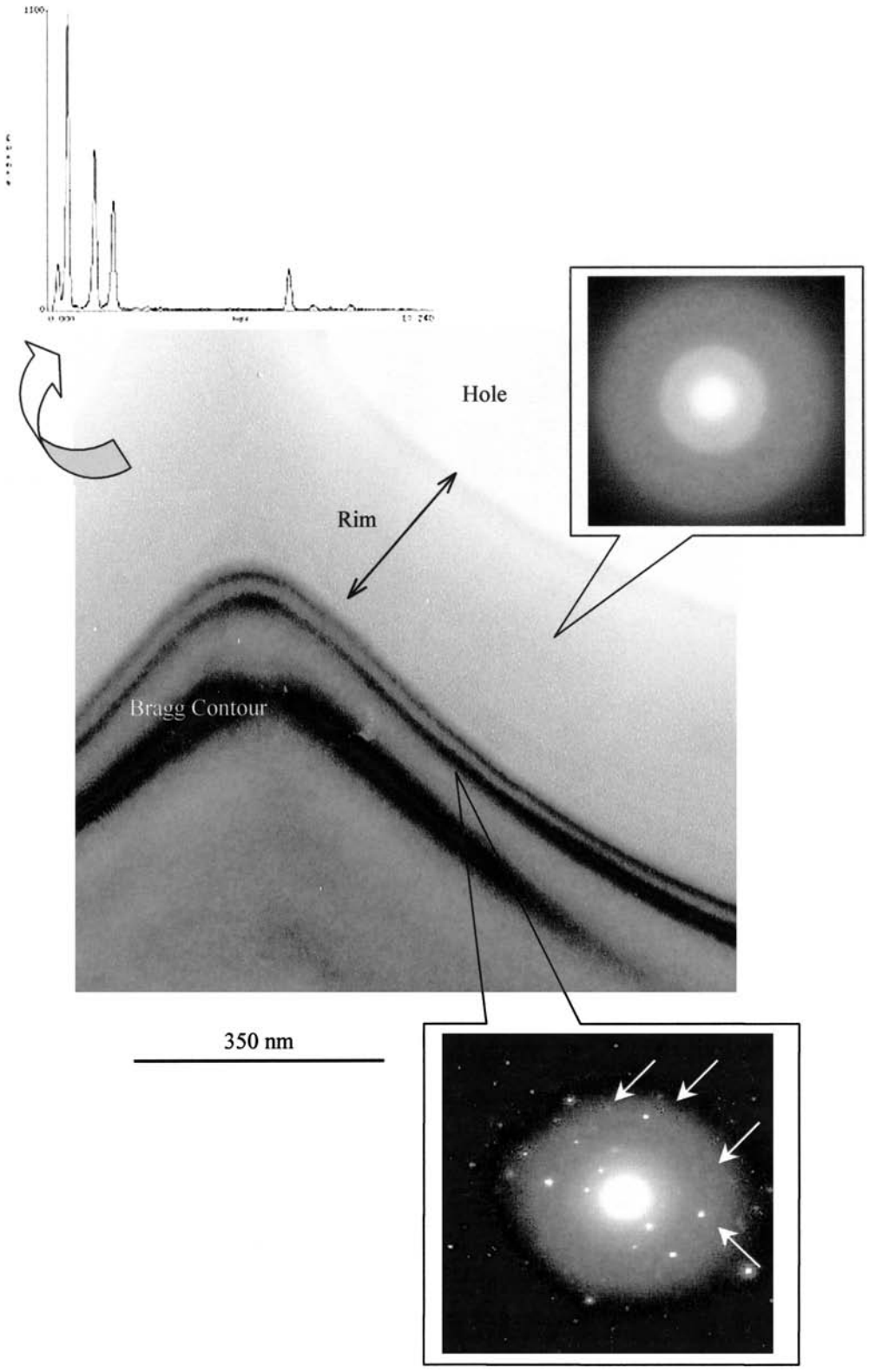


FIG. 2. Typical features of irradiated sample as observed at the TEM (here sample #3, irradiated with 4 keV He^+, fluence 5×10^{16} ions/cm^2). The sample is seen in plan view; it exhibits dark fringes corresponding to crystalline matter in Bragg position. The rim without any contrast is characteristic of an amorphous region. Diffraction (in the top right corner) confirms that the rim is amorphous. In thicker part, diffraction (bottom) reveals the superposition of amorphous compounds with the initial olivine. An EDS spectrum recorded on the rim confirms that olivine elements are presents.

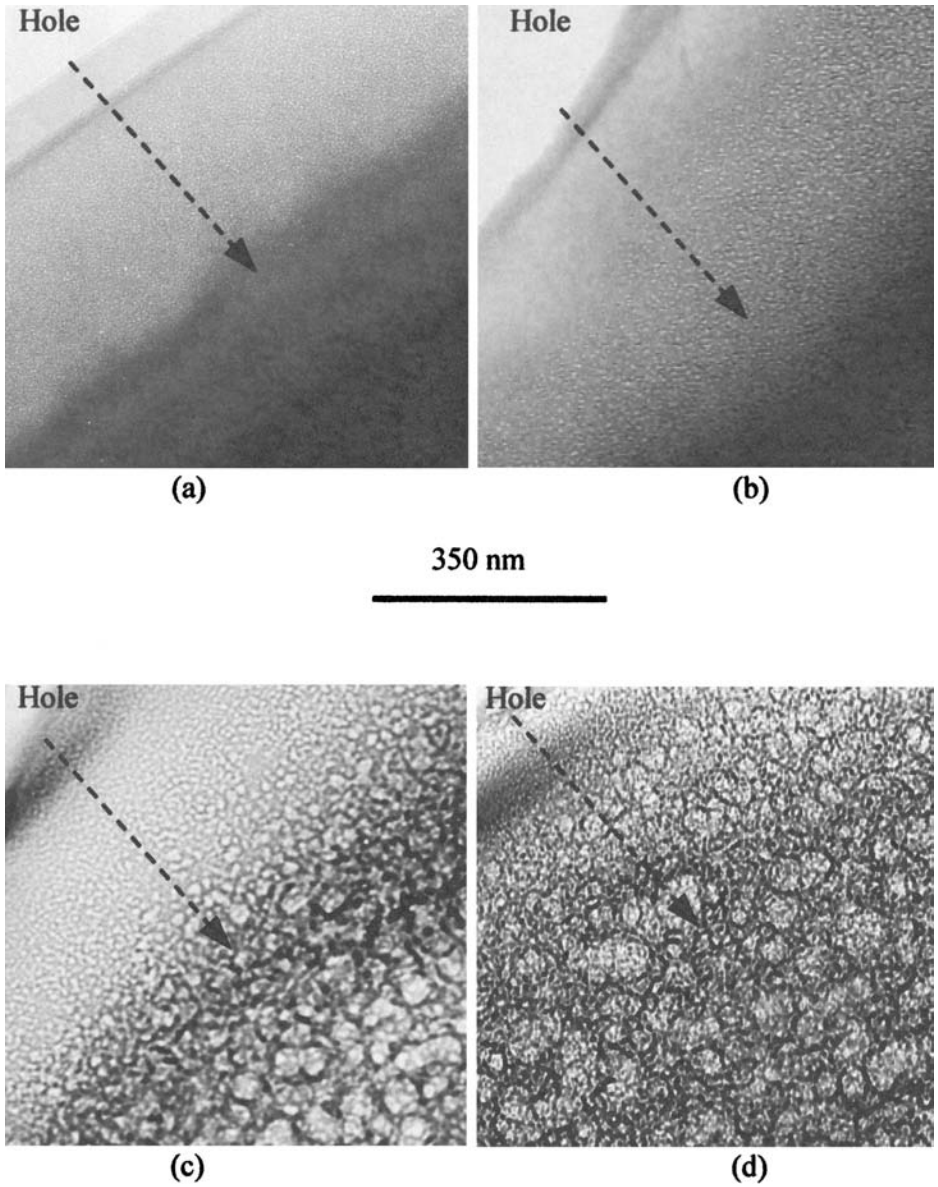


FIG. 3. TEM bright-field images from four samples (irradiated at 4 keV with different fluences: (a) 5×10^{16} He^+/cm^2, (b) 10^{17} He^+/cm^2, (c) 5×10^{17} He^+/cm^2, (d) 10^{18} He^+/cm^2). In these plan views, upper left corners correspond to the edge of the sample and arrows indicate the increasing thickness. A large amount of bubbles are visible with a mean size of bubbles increasing as fluence is higher.

on Fig. 2) adjacent to the amorphous rim show normal spot patterns characteristic of olivine with still some diffuse rings superimposed to them. These diffuse rings are no more visible when SAED patterns are recorded in thicker regions.

The second feature corresponds to numerous gas bubbles or voids that are pervasive in the crystalline regions and extend partly into the amorphous rim. These bubbles are more easily seen on samples irradiated at higher fluences, although they can be seen in sample #3 if the magnification is increased (see Fig. 3a). Figure 3 shows that the mean size of the bubbles increases with the irradiation fluence. Only the thinnest part of the rim is free of bubbles. Figure 4a,b shows that very similar features are present in samples #8 and #9 irradiated with more energetic ions (10 and 50 keV, respectively). The only difference might stem from the width of the bubble-depleted region near the edge of the sample which increases with increasing energies, as well as the width of the amorphous region.

Chemical Evolution

We have investigated the chemical composition of the amorphous rim produced by the irradiation. We have performed line profiles from the tip of the rim to thicker areas. Figure 5

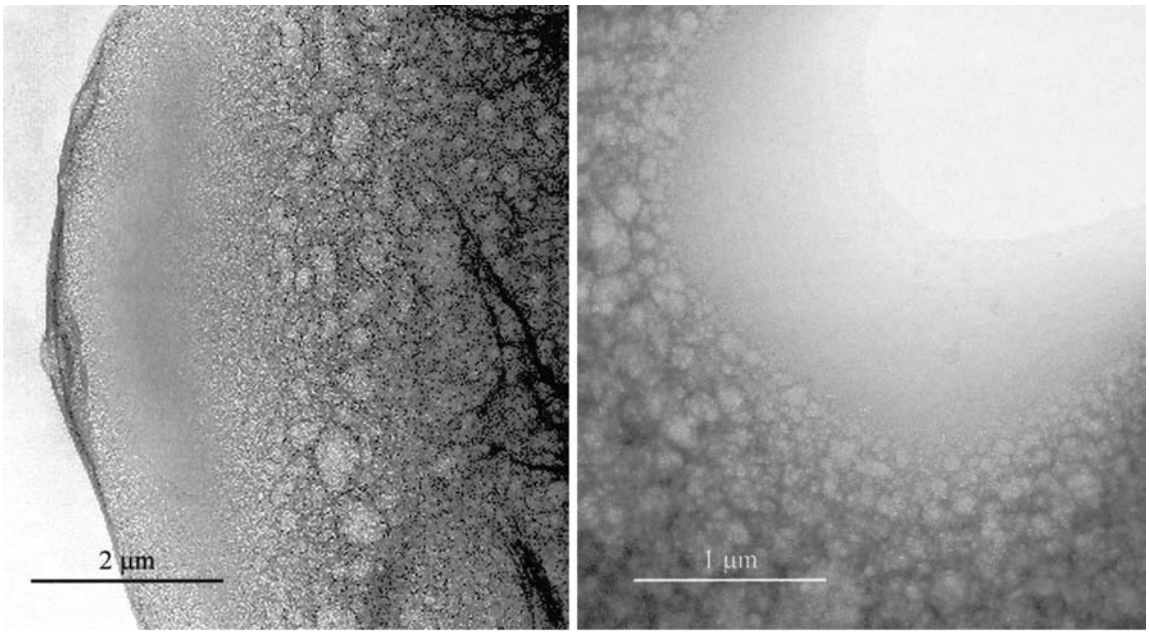


FIG. 4. TEM micrographs of irradiated samples with a fluence of 10^{18} ions/cm^2. (a) 10 keV irradiation (sample #8) and (b) 50 keV irradiation (sample #9). Note the rim near the edge, which corresponds to the ion-transparent region of the sample. Compared to a 4 keV irradiation, the width of the bubble-depleted region is larger.

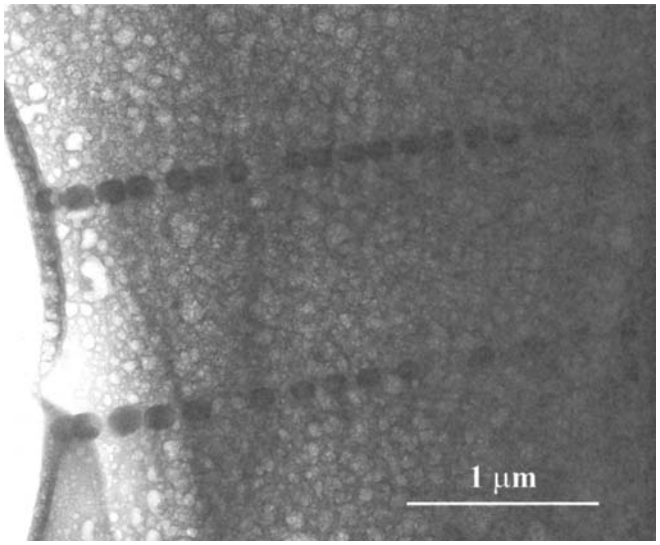


FIG. 5. Bright-field TEM image of sample #5 after chemical characterization. Black dots visible on the image are contamination spots and represent locii of analyses. EDS analyses were performed from the edge of the specimen to thicker regions.

presents a TEM micrograph illustrating the measurement: the black spots are the locii (sample #5) where the probe was positioned for individual analysis; they are due to contamination. The composition profile corresponding to this micrograph is displayed in Fig. 6, in which is also plotted for comparison a line profile into non-irradiated olivine using exactly the same experimental procedure (samples #5 and #0). It is important to remember at this stage that the quantification in the TEM requires a precise determination of the thickness at the exact probe location. With the line profile being recorded on a bevel-shaped specimen, this parameter varies at each point. The thickness determination in silicates is usually obtained following the procedure proposed by Van Cappellen and Doukhan (1994). However, this method is based on the crystal chemistry of the specimen which is shown here to deviate significantly from stoichiometry at the rim (Fig. 6). A specific procedure has been developed to overcome this problem and is described in the appendix. Figure 6 shows that, compared to the non-irradiated sample, a composition profile develops in the amorphous rim formed in samples irradiated at 4 keV. This composition profile corresponds to a deviation of both the O/Si and the Mg/Si ratio from their initial values (O/Si = 4 and Mg/Si = 1.8, characteristic of our San Carlos olivine). Above a fluence of 5×10^{16} He$^+$/cm^2, all samples exhibit such a composition profile. It is more and more pronounced when the fluence increases. Figure 7 shows the composition reached at a given arbitrary thickness as a function of the increasing fluence (data are extracted from profiles similar to Fig. 6). At a given fluence (10^{18} ions/cm^2), the profile is even more marked when the irradiation energy is increased from 4 to 10 keV (Fig. 8). However, the sample irradiated at 50 keV has an amorphous rim that exhibits no significant deviation from the olivine stoichiometry (Fig. 8).

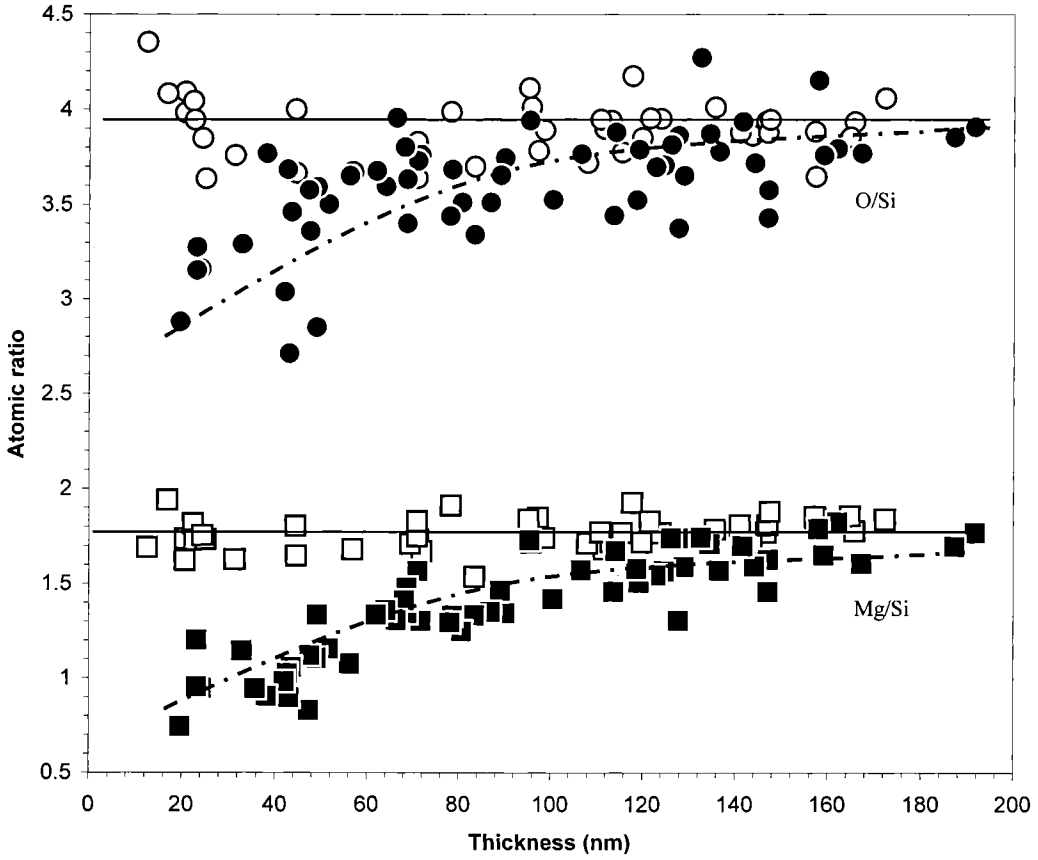


FIG. 6. Composition profile of an irradiated olivine (here sample #5, filled marks) compared with a similar profile recorded on a non-irradiated sample (sample #0, open marks). Atomic ratio O/Si (circle) and Mg/Si (rectangle) are plotted against thickness. The solid curves, for guidance only, indicate a strong fractionation in thin area.

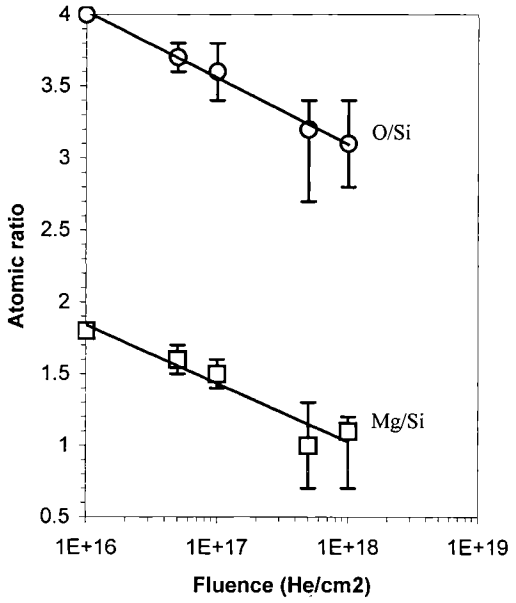


FIG. 7. Results of 4 keV irradiations (samples #3, #4, #5 and #6) plotted as the evolution of O/Si (circle) and Mg/Si (rectangle) atomic ratios function of fluences. Atomic ratios are those reached in 30 nm thick region. Amounts of chemical damages are increasing as fluences are higher.

X-Ray Photoemission Spectroscopy

XPS data confirm the chemical information derived from analytical TEM study. Indeed, 4 keV He^+ irradiation is found to induce decreasing O/Si and Mg/Si ratios below the surface (see Table 2). In addition, XPS provides information on iron and its valence state that cannot be extracted from ATEM. Figure 9 shows a detail of the XPS spectra in the Fe_{2p} region for both the reference (non-irradiated) and irradiated sample (#7). It shows that prior to irradiation, iron is in the ferrous (Fe^{2+}) state in the sample, according to the Fe_{2p} photopeak profile showing a 6 eV separation between the main line and the satellite structure (Maschhoff and Armstrong, 1991). After bombarding the sample with ~10^{17} He^+ ions/cm^2, the two peaks characteristic of iron in the metallic state $Fe_{2p1/2}$ and $Fe_{2p3/2}$ (at 720.2 and 707 eV, respectively) appear showing that iron has been reduced during irradiation. The ratio Fe^0/Fe^{2+} is then determined by spectra difference, considering the defined criteria: energy alignment, baseline removal and area normalization. The reduction effect is significant, the difference in the two spectra reveals that more than 40% of the native Fe^{2+} iron atoms have been reduced to Fe^0.

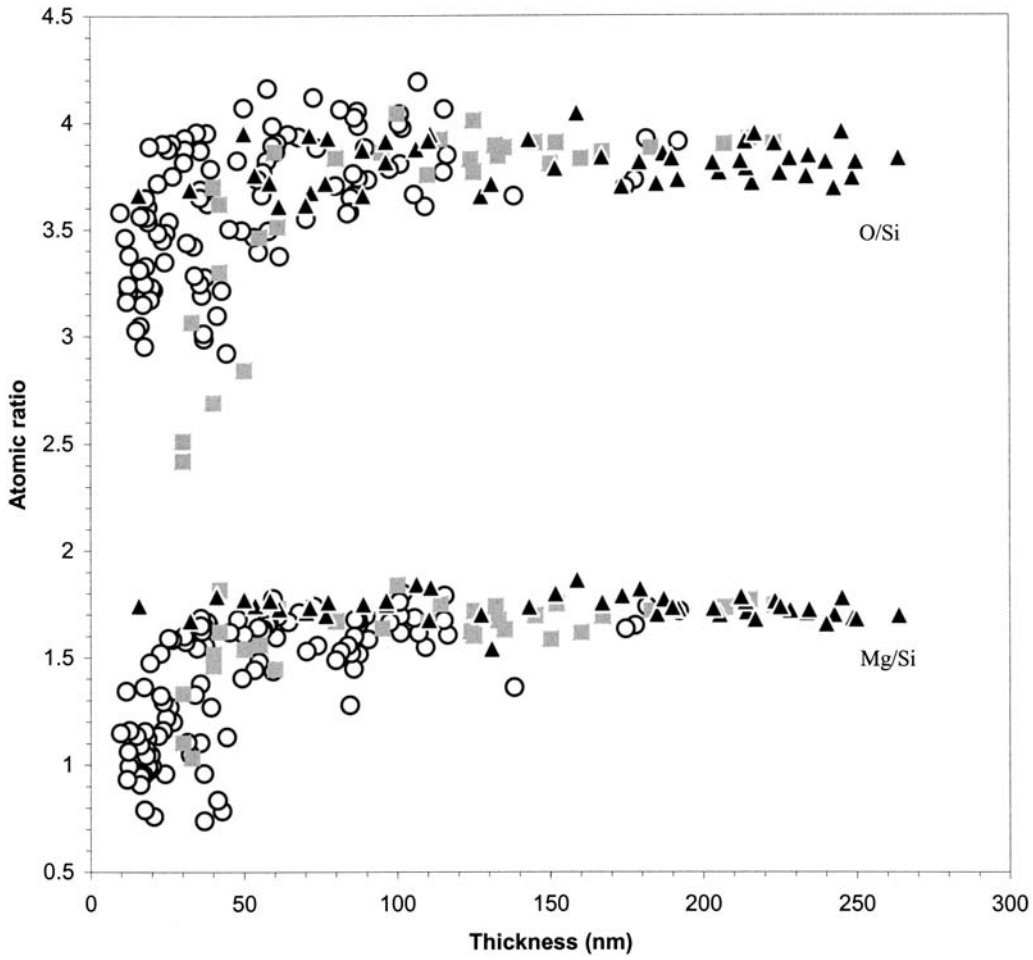


FIG. 8. Evolution of composition profiles for the three different energies: 4, 10 and 50 keV, with same fluence of 10^{18} ions/cm^2 (sample #6, open circles; sample #8, grey squares; sample #9, black triangles, respectively). One notes that a 50 keV irradiation does not induce detectable chemical changes.

TABLE 2. Results of XPS analysis (sample #7).*

Sample	O/Si (atomic ratio)	Mg/Si (atomic ratio)	Fe_0/Fe_{tot} (%)
Reference	3.8	1.7	0
He^+ irradiated	3.1	1.4	43

*The amount of reduced iron is deduced by spectra difference of the XPS data (as explained in text).

DISCUSSION

Structural Evolution: Crystalline to Amorphous Transition

It is well known that ion irradiation causes amorphization in a large number of materials. When an ion goes through the target it loses its energy by electronic (ionization) and nuclear (elastic collision) interaction (*e.g.*, Weber *et al.*, 1998, and references therein). Nuclear interactions are found to predominate for a low ion velocity while ionization occurs

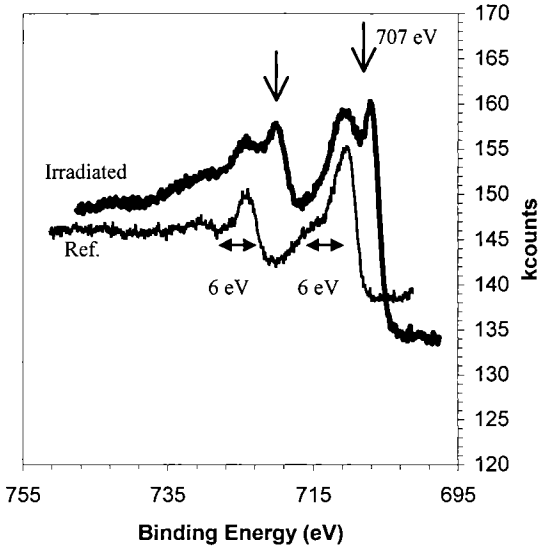


FIG. 9. Comparison of XPS spectra for iron. After He^+ irradiation, a part of FeO is reduced into metallic iron as revealed by the appearance of new peaks characteristic of Fe^0.

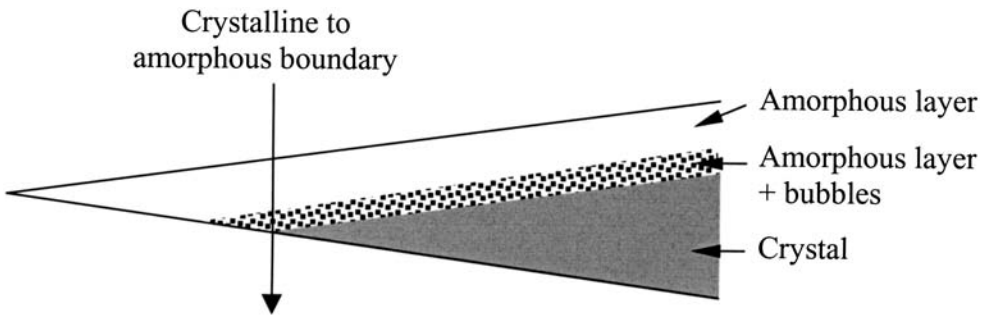


FIG. 10. Schematic view of a TEM sample after irradiation. The specimen is composed of three different layers. On the top, there is an amorphous layer above the region of helium implantation. Below these two highly damaged layers, one finds the initial and undamaged olivine crystal.

mostly at high velocity. In our experiments He^+ irradiation were performed at low energy, for which there is a predominance of nuclear interaction with the target atoms. The series of experiments performed with 4 keV He^+ ions under various fluences shows that above a fluence of 5×10^{16} ions/cm^2, the surface exposed to the ion beam (*i.e.*, the upper surface layer) is fully amorphous. Below this fluence, the samples remain crystalline although some defects are present. They probably reflect a progressive crystalline to amorphous transformation. Amorphization occurs as consequence of the direct collisions of the incident He^+ ions with the target atoms. Each incident ion gives rise to a displacement cascade at the end of the implantation track, leading to the formation of an amorphous region by local collapse of the crystalline structure. The average number of atomic displacement produced per He implantation event can be evaluated with the Monte Carlo computer code TRIM (TRansport of Ions in Matter; Ziegler *et al.*, 1996). Assuming a displacement energy of 25 eV for all species (Wang *et al.*, 1999), there were ~40 (4 keV), 70 (10 keV) and 120 (50 keV) atomic displacements per He implantation. The completely amorphous state is the consequence of accumulation and overlap of the individual events. Our experiments on 4 keV He^+ irradiation determine a critical fluence for amorphization in between 10^{16} and 5×10^{16} He^+/cm^2.

This amorphization process has been intensively studied in a large number of materials, including olivine (Wang *et al.*, 1993, 1999, 2000; Eby *et al.*, 1996). These authors (Wang *et al.*, 1993, 1999; Eby *et al.*, 1996) have found a critical fluence ~5×10^{14} ions/cm^2 with Kr^+ ions at 1.5 MeV. By fitting the projectile ion and the associated number of atomic displacements per incident ion we find that this value is comparable with our results. Indeed, such experimental conditions (Kr^+ at 1.5 MeV) significantly increase the size of displacement cascade. Thus, it is not surprising to find a higher critical fluence for amorphization when less energetic ions are involved.

Only the top of the samples is exposed to the He^+ ions. Because of the bevel-shaped geometric configuration the amorphous material can be observed solely at the edge of the sample. In thicker areas the amorphous layer is superimposed to the undamaged olivine. The geometric configuration after irradiation is shown in Fig. 10. The thickness of the amorphous layer can be measured by placing the probe at the boundary between the amorphous rim and the "crystalline" region (see Fig. 10) and by recording an EDX spectrum. The procedure, described in "Transmission Electron Microscope Characterization" and in the appendix, yields the thickness of the specimen at this point and is the thickness of this amorphous layer. We find 45 ± 15 nm at 4 keV and 90 ± 15 nm at 10 keV. At 50 keV the thickness of the amorphous layer is larger than 200 nm but this has not been accurately measured. These values compare well with TRIM calculations, for which we have found 40, 95 and 380 nm for 4, 10 and 50 keV, respectively (Table 3 and Fig. 11).

Helium Bubble Formation

The second feature seen in the images is the bubbles or voids. They are absent at the extreme tip of the thin foils. This suggests that they form a layer at the bottom of the amorphous layer (see Fig. 10). For the 10 and 50 keV irradiations most of the He^+ ions are transmitted through the edge of the bevel of the samples. In these thin areas the He concentration might be very low. On the TEM micrographs we observed that the bubble density near the edge is very low. Different fluences have been tested for a 4 keV energy. Because of this low energy, the free rim is very narrow. This series of samples allows observing the bubble size evolution. The volume fraction of these bubbles, as well as their size, increase

TABLE 3. Comparison between experimental determination of the amorphous thickness and penetration depths results of TRIM calculations.

Ion energy	Thickness of the amorphous layer (nm)	Penetration depths of the ions calculated by TRIM (nm)
4 keV	45 ± 15	40
10 keV	90 ± 15	950
50 keV	n.d.	380

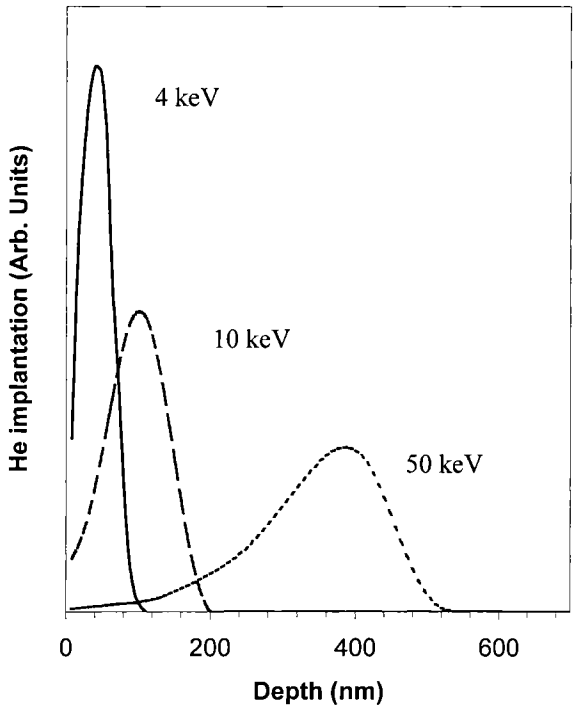


FIG. 11. Results of helium implantation calculated with TRIM for 4, 10 and 50 keV irradiation.

with the He^+ fluence received. All these pieces of evidence, together with the free bubble rim in samples irradiated at 10 and 50 keV, suggest that bubbles are filled with He gas. The bubbles show no sign of over-pressurisation (internal stresses, cracks, *etc.*) showing that relaxation of the olivine matrix has occurred. The growth of the bubbles with the increasing fluence requires some matter to be excavated to make space available. These precipitation and growth mechanisms show that diffusion of olivine species at room temperature must be assisted by irradiation. Formation of He bubbles after He^+ irradiation has already been reported in numerous studies (*e.g.*, Johnson *et al.*, 2000 for insulating ceramic; Raineri *et al.*, 2000; Sasajima *et al.*, 1999 for Al_2O_3).

All experimental evidence and the scheme presented in Fig. 10 are in good agreement with TRIM calculation. Indeed, results of TRIM on the penetration depth of He^+ ions in olivine and He implantation are displayed in Fig. 11 and in Table 3. They show that the amorphized layer corresponds to the penetration depth of the ions and that the bubble layer is located at the depths at which the ions stop in the specimen.

Chemical Modification

Our study has shown that He^+ irradiation induces a chemical fractionation below the exposed surface. This chemical evolution with the He^+ fluence has been particularly documented in case of 4 keV He^+ ions (samples #1 to #7) for which a composition gradient has been shown when the fluence exceeds 10^{17} ions/cm^2. This chemical evolution is induced by collisions between the incident He^+ ions and the target. Let us consider a displacement event occurring near the surface of the sample. If the energy gained during the collision by the target atoms is sufficient they can escape through the surface into vacuum. This process, called sputtering, depends on the energy of incident ions, the atom masses of both the projectile and the target, the displacement energies, the binding energies and the surface binding energy of the target atoms (see Smentkowski, 2000, for details). The sputtering yield is the mean number of sputtered target atoms per incident ion. It depends on which lattice atom is knocked. For example, in olivine, Mg or O will be more sensitive to sputtering than Si and Fe. This effect can be responsible for chemical fractionation by removing some species preferentially. The sputtering yields for O, Mg, Si and Fe were determined using TRIM calculation.

The various parameters used for this calculation are the displacement energies E_d, the lattice binding energies E_b and the surface binding energies E_s. The displacement energies are known only for a few materials and not for olivine. We have taken the approximation $E_d = 25$ eV proposed by Wang *et al.* (1999). We set the E_b value at 2 eV for each element (Eby *et al.*, 1996). For the surface binding energy of an atom to a surface, again known only for a few materials, it is common to use the heat of sublimation as an estimate (Ziegler *et al.*, 1996), for our olivine, $E_s = 5.6$ eV. One specific detail of our calculation is the particular geometric configuration we used for the irradiations. The samples can be considered as ultra-thin sample, in which two free surfaces are present. The results of TRIM calculations are shown in Fig. 12. This figure shows the evolution of total sputtering yield (O + Mg + Si + Fe) with the sample thickness for the three acceleration voltages used in the present study, assuming thin samples with parallel surfaces. As expected, sputtering is found to be more and more important as helium incident energy decreases (*i.e.*, when nuclear collision effects are predominant). These calculations highlight also the influence of the free surfaces in the sputtering efficiency. Indeed, it is found that sputtering is significant for thin samples only for which displaced atoms have a chance to escape from the specimen through a nearby surface. This explains also why sputtering is negligible for 50 keV ions (Fig. 8) for which displacements occur at greater depths, that is far from the surface. The maximum sputtering yield is also found to evolve with He incident energy. The maxima are found at around 40, 90 and 400 nm for 4, 10, 50 keV, respectively; in other words for thickness very close to the implantation distances, where the nuclear interaction are maximum.

Using modelled sputtering yields, we can calculate the composition profile which is expected to result from sputtering from a bevel-edge TEM sample subjected to a given irradiation (*i.e.*, with an increasing thickness for a direct comparison with our experimental results in the ATEM profiles; see Figs. 1 or 10). Figure 13 shows the comparison between such a simulation

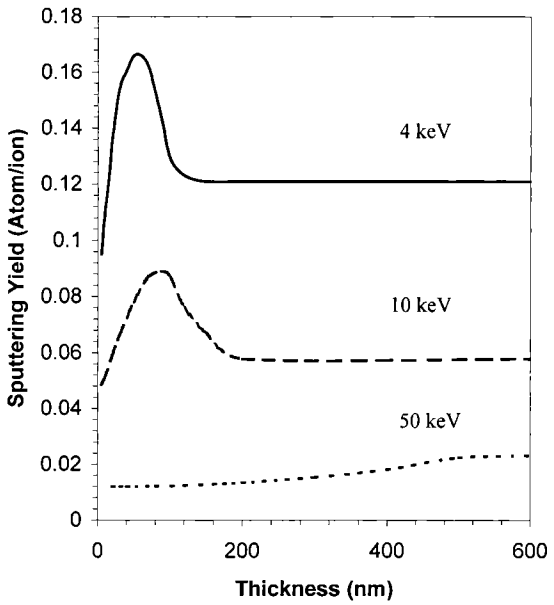


FIG. 12. Total sputtering yields calculated by TRIM plotted as a function of the sample thickness. Sputtering yields are found to be higher for 4 or 10 keV irradiations compared to the 50 keV irradiation. Note that sputtering is strongly enhanced for thicknesses comparable to implantation depths.

based on TRIM and our experimental results in case of sample #6 irradiated with 10^{18} ions/cm^2 at 4 keV. It shows that nuclear collision-induced differential sputtering can account for the O and Mg depletion below the surface, and that the amount of fractionation as well as the extent of the profile are in good agreement with the experimental results at 4 keV. The influence of the fluence, which gives deeper and steeper composition profiles, is also well reproduced (Fig. 14). However, at 10 keV, the experimental composition profile is more pronounced than the one predicted by simulation (see Fig. 15). This underestimation suggests that another process might contribute to chemical fractionation. This process might be due to ionization which has been shown to induce chemical modification in olivine (Carrez *et al.*, 2001 in the case of high-velocity electrons). In the case of 50 keV ions, the sputtering yield is very low and the influence of the thickness described in the previous paragraph can explain why the model predicts no composition profile to form, in agreement with our experimental results (Fig. 16).

Finally, TRIM calculations show that the sputtering yield for iron atoms is negligible, whatever the irradiation conditions. We thus assume that iron stays in the sample. As oxygen is removed, iron is progressively reduced. This reduction process has previously been reported by Dukes *et al.* (1999). These

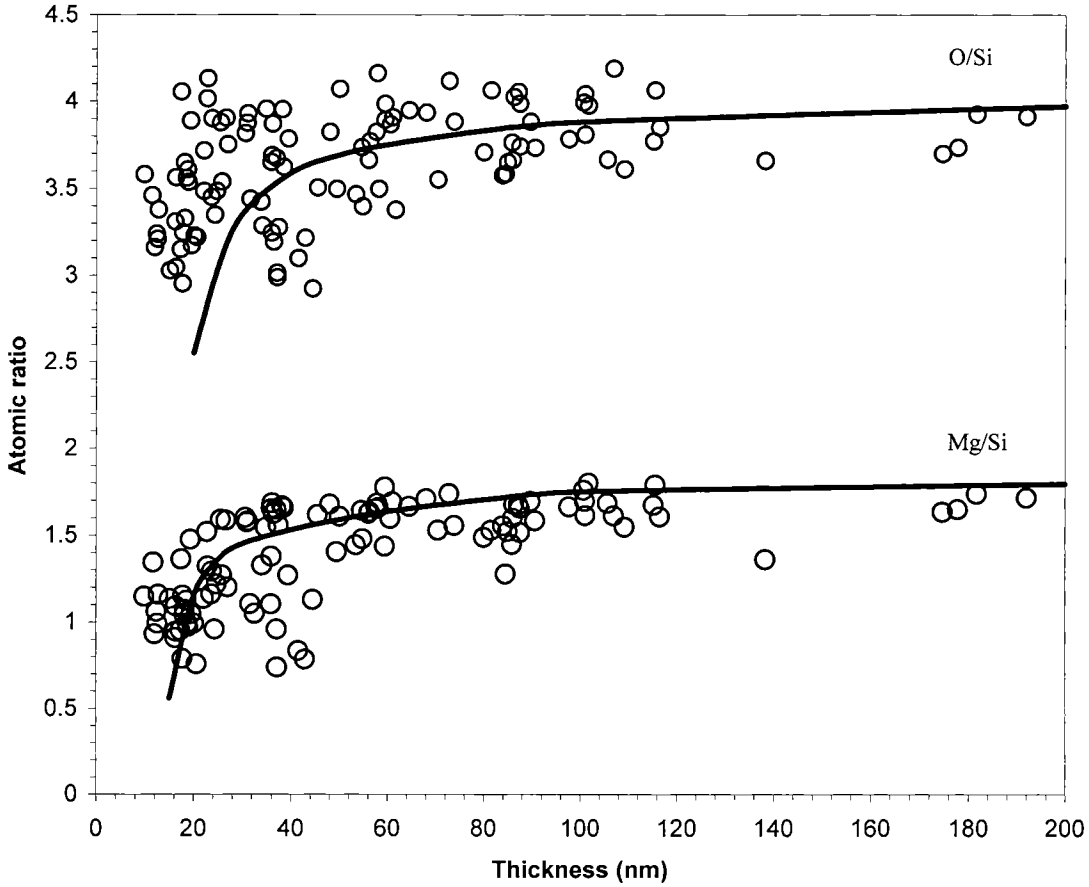


FIG. 13. Comparison of TRIM calculated chemical profile and experimental data. Data come from sample #6 and the calculations (solid lines) are obtained with a fluence of 10^{18} He^+/cm^2.

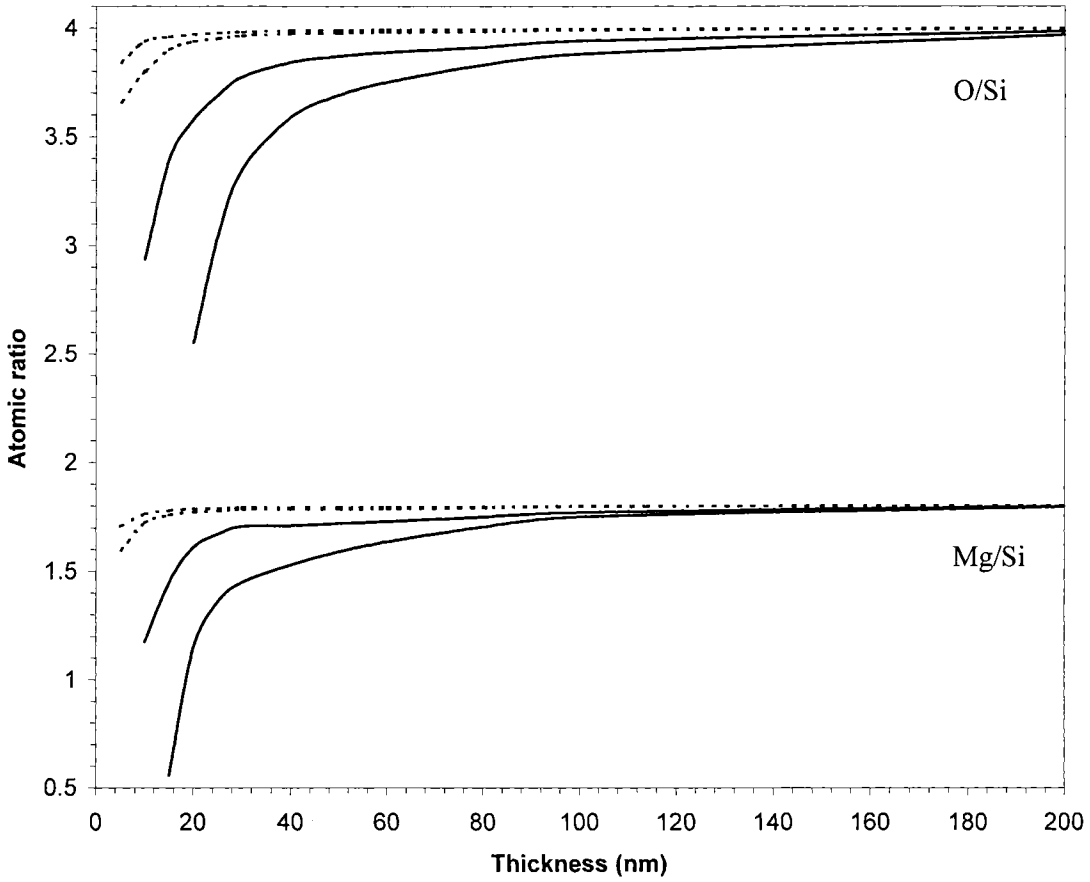


FIG. 14. Chemical profiles derived from TRIM calculations. For a 4 keV irradiation, atomic ratios are presented for 5×10^{16} (upper dash lines), 10^{17} (lower dash lines), 5×10^{17} (upper solid lines) and 10^{18} ions/cm^2 (lower solid lines).

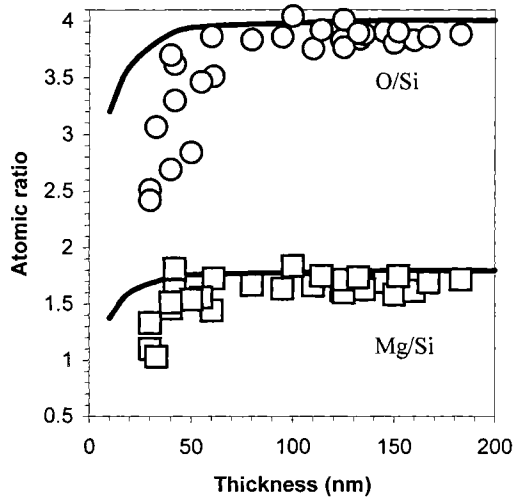


FIG. 15. Comparison of calculations profile (solid lines) with experimental ones for a 10 keV irradiation (samples #8). Even if the trend is respected, experimental data seems to deviate from simulations.

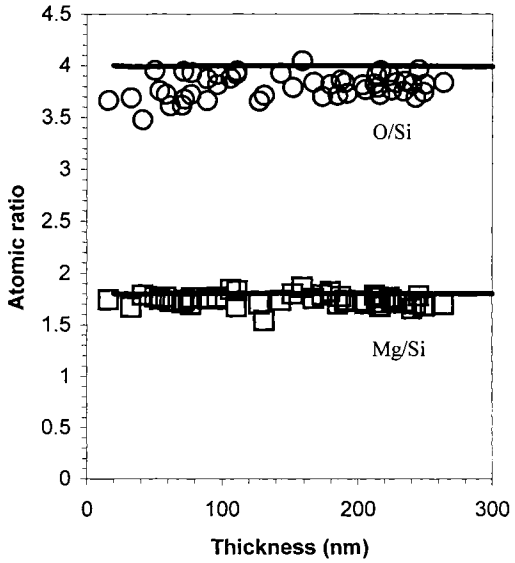


FIG. 16. Composition profiles for a 50 keV irradiation. Experimental data (sample #9) are compared to TRIM simulations (solid lines). No chemical changes are observed, either for the experimental plot or for the simulation.

authors found that under similar experimental conditions (4 keV He^+ irradiations) there was a reduction of iron and silicon. If our experiments lead to a large amount of reduced iron, no evidence for silicon reduction were found. Nevertheless, the amount of reduced Si evidenced by Dukes *et al.* (1999) was relatively low.

ASTROPHYSICAL IMPLICATIONS

Interstellar silicate dust is subjected to numerous processes in different astrophysical environments (*e.g.*, interaction with cosmic rays, photons, electrons and ions accelerated by supernovae shock waves). The small size (typically 200 nm) renders the bulk of the dust particularly sensitive to irradiation. A number of experiments have been performed to infer the structural and chemical changes induced by the irradiation of silicates (*e.g.*, Borg *et al.*, 1982; Bradley, 1994; Keller and McKay, 1997; Dukes *et al.*, 1999; Wang *et al.*, 1999; Demyk *et al.*, 2001; Carrez *et al.*, 2001). These changes generally include amorphization and chemical fractionation but the nature of the irradiation-induced effects strongly depends on the incident particles, their energy and their fluence. Most of these works are dedicated to the study of solar wind interactions with interplanetary dust particles (IDPS) or with lunar regolith (*e.g.*, Borg *et al.*, 1982 or Keller and McKay, 1997). Nevertheless, these experiments are also relevant to the study of irradiation of dust in interstellar medium conditions since they deal with ions, energies and fluences that can be found in shocked regions of the diffuse interstellar medium (Jones *et al.*, 1996; Demyk *et al.*, 2001). The results presented here are thus also interesting for the study of the effects induced by the solar wind. For example, the presence of helium bubbles implanted in our irradiated samples confirms the hypothesis of Brownlee *et al.* (1998) who observe bubbles in IDPs which they suspect to result from helium implantation due to solar wind irradiation.

In the case of interstellar dust, interaction with light particles ionized and accelerated in supernovae shocks is thought to be one of the predominant process (Jones, 2000; Demyk *et al.*, 2001). The propagation of a supernova shock wave in the diffuse interstellar medium ionizes the gas mainly composed of H and He, and accelerates the ions to different energies depending on the velocity of the shock. For example, a 430 km/s velocity shock accelerates a column of gas of $\sim 10^{17}$ He^+/cm^2 with an energy of 4 keV (Jones *et al.*, 1996). In this study, olivine undergoes amorphization for a 4 keV He^+ fluence of between 10^{16} and 5×10^{16} ions/cm^2. Thus, relatively high-velocity shocks (V > 200 km/s) are efficient to amorphize olivine dust.

In addition to the structural evolution, our experiments also evidence a chemical fractionation, with a preferential loss of O and Mg. Such changes have been previously observed by Bradley (1994) with proton irradiation or by Dukes *et al.* (1999) for helium irradiation. The specificity of our experiments is the geometrical configuration we use since the irradiation is performed on pre-thinned TEM samples. The samples thus have a high surface/volume ratio. Although non-spherical, the beveled shape with continuously varying thickness is suitable for studying size effects during an irradiation process and a given thickness can be compared to a dust surface/volume ratio expected from interstellar grains. Thin regions are very sensitive to irradiation and exhibit the stronger chemical changes. This comes from the fact that the efficiency of the sputtering process is increased by the presence of free back surface. As a result, not only the "classical" sputtering from the top surface operates, but nuclear collisions occurring in the bulk can provide enough energy to target atoms to escape through the back surface and thus increase the amount of sputtered elements. Consequently, for a 4 keV He^+ irradiation, chemical changes are twice more important for 40–50 nm sized grains compare to larger grains. More generally, in shocks, dust grains having a size comparable to the penetration depth of the incident ions will undergo an important differential sputtering leading to chemical fractionation. The composition of these irradiated silicates grains will then tend toward a pyroxene-type composition (characterized by atomic ratios O/Si = 3 and Mg/Si = 1). This kind of chemical evolution is in agreement with the evolution of interstellar silicates. Indeed, around protostars where grains end their life after their passage though the interstellar medium, the silicates are observed to be predominantly pyroxene (Dorschner *et al.*, 1988; Bowey *et al.*, 1998; Demyk *et al.*, 1999) whereas their initial composition, as observed in ABG stars, is mostly olivine.

The sputtering experienced during the irradiation process is not stoichiometric. In particular, iron is not strongly sputtered; it appears to be reduced and becomes metallic in the irradiated samples. Iron may be an abundant constituent of the dust as it is approximately as abundant as silicon (Snow and Witt, 1996). However, the nature of its incorporation into the dust is still a matter of debate. Several possibilities exist such as the existence of oxide dust grains or inclusions in silicates grains or the existence of pure metallic iron grains or inclusions into silicates (Kemper *et al.*, 2002). It could also be part of the structure of silicates in the form of Fe-rich silicates (Tielens *et al.*, 1990; Molster *et al.*, 2002). The results presented here show that, if iron is indeed in silicate grains, it will tend, under irradiation in the interstellar medium, to remain in the matrix of the grain in a metallic form. Furthermore, since the silicate matrix simultaneously loses Mg and O by sputtering, the grains will tend to be enriched in Fe. The grains are then expected to be iron enriched and to contain metallic iron inclusions after a prolonged sojourn in the interstellar medium.

Part of the grains will end up in the circumstellar disks around young stars as well as in planetary systems such as ours. Pristine material possibly originating from comets are extensively studied in the laboratory. In particular a good piece of information comes from studies of IDPs (Bradley *et al.*, 1999). Our results concerning the chemical fractionation do qualitatively agree with the observation of preponderance of

pyroxene over olivine amongst chondritic porous IDPs (Bradley, 1988; Messenger, 2000), as well as in comets (Wooden *et al.*, 1999; Wooden, 2002). Since olivine appears to be the dominant phase in AGB stars, ion bombardment of these grains in the interstellar medium could explain the change in mineralogy to that for the most interstellar medium like IDPs (Wooden *et al.*, 2000). In addition, the observed porosity in our irradiated samples may help to understand the high porosity of the silicates components deduced from analysis of Hale Bopp's spectra (Harker *et al.*, 2002), using a thermal model in which the porosity is an important property. Similarly, our results suggest that the presence of Fe and FeS nanoparticles in glass with embedded metal and sulfides (GEMS) (Bradley *et al.*, 1999) could well be the results of ion irradiation either in the interstellar medium or from early solar winds.

CONCLUSIONS

He^+ irradiation has been performed on thin olivine $Mg_{1.8}Fe_{0.2}SiO_4$ samples to simulate the physical and chemical effects of supernovae shocks on dust grains travelling in the interstellar medium. Our results can be summarized as follows:

(1) Amorphization of olivine occurs due to nuclear collisions with low-energy helium ions.

(2) Chemical changes are observed under 4 and 10 keV irradiation with a decrease of the atomic ratios O/Si and Mg/Si (from 4 to 3 and 1.8 to 1, respectively). Differential sputtering is at the origin of these damages.

(3) Reduction processes are also expected with the appearance of metallic iron.

(4) The role of the surface, and thus of the dust size, is emphasised in the sputtering process.

(5) The evolution of silicate grains in supernova shocks, as expected from our results, is consistent with the observed structural and compositional evolution of silicates in the interstellar medium (*i.e.*, from olivine-type to pyroxene-type composition), as indeed observed thanks to recent ISO short wavelength spectrometer measurements.

The structural and chemical changes indicated in our experiments are compatible with the observed evolution of silicate dust grains in the interstellar medium, that is, the amorphization of the crystalline dust and the shift in its composition from olivine- to pyroxene-type silicate while passing from their site of production (late-type stars) to their site of destruction (early-type stars/last stage of molecular cloud evolution). Furthermore, we find that grains having sizes on the order of and smaller than the penetration depth of the incident ions will be the most chemically altered. In addition, grains having a size on the order of, and smaller than twice the penetration depth of the incident ions will be completely amorphized throughout their entire volume. Thus, considering the ion fluences at which theses changes occur in our experiments, the propagation of supernovae shock waves through the interstellar medium will efficiently alter the physical state of dust through the effects of shock-accelerated incident ion irradiation experienced by interstellar grains during their lifetime in our galaxy.

Acknowledgments–The authors thank the CSNSM (Orsay) for having performed the irradiation experiments on the thin samples. We also thank D. H. Wooden and an anonymous reviewer for constructive comments. Supports from the "Programme National de Planétologie" (PNP-CNRS) and from the program "Physique et Chimie du Milieu Interstellaire" (PCMI-CNRS) are also acknowledged.

Editorial handling: D. Prialnik

REFERENCES

BORG J., BIBRING J. P., COWSIK R., LANGEVIN Y. AND MAURETTE M. (1982) A model for the accumulation of solar wind radiation damage effects in lunar dust grains (abstract). *Lunar Planet. Sci.* **13**, 59–60.

BOWEY J. E., ADAMSON A. J. AND WHITTET D. C. B. (1998) The 10-μm profile of molecular-cloud and diffuse interstellar medium silicate dust. *Mon. Not. R. Astron. Soc.* **298**, 131–138.

BRADLEY J. P. (1988) Analysis of chondritic interplanetary dust thin-sections. *Geochim. Cosmochim. Acta* **52**, 889–900.

BRADLEY J. P. (1994) Chemically anomalous preaccretionally irradiated grains in interplanetary dust from comets. *Science* **265**, 925–929.

BRADLEY J. P., SNOW T. P., BROWNLEE D. E. AND HANNER M. S. (1999) Mg-rich olivine and pyroxene grains in primitive meteoritic materials: Comparison with crystalline silicate data from ISO. In *Solid Interstellar Matter: The ISO Revolution* (eds. L. d'Hendecourt, C. Joblin and A. Jones), pp. 297–315. EDP Sciences and Springer-Verlag, Paris, France.

BRUCATO J. R., COLANGELI L., MENNELLA V., PALUMBO P. AND BUSSOLETTI E. (1999) Mid-infrared spectral evolution of thermally annealed amorphous pyroxene. *Astron. Astrophys.* **348**, 1012–1019.

BROWNLEE D. E., JOSWIAK D. J., BRADLEY J. P., SCHLUTTER D. J. AND PEPIN R. O. (1998) Tiny bubbles: Direct observation of He in IDPs (abstract). *Lunar Planet. Sci.* **29**, #1869, Lunar and Planetary Institute, Houston, Texas, USA (CD-ROM).

CARREZ P., LEROUX H., CORDIER P. AND GUYOT F. (2001) Electron-irradiation-induced phase transformation and fractional volatilization in $(Mg,Fe)_2SiO_4$ olivine thin films. *Philos. Mag.* **A81**, 2823–2840.

CARREZ P., DEMYK K., LEROUX H., CORDIER P., JONES A. AND D'HENDECOURT L. (2002) Low-temperature crystallization of $MgSiO_3$ glasses under electron irradiation: Possible implications for silicate dust evolution in circumstellar environments. *Meteorit. Planet. Sci.* **37**, 1615–1622.

CROVISIER J., LEECH K., BOCKELEE-MORVAN D., BROOKE T. Y., HANNER M. S., ALTIERI B., KELLER H. U. AND LELLOUCH E. (1997) The spectrum of comet Hale–Bopp (C/1995 01) observed with the infrared space observatory at 2.9 AU from the Sun. *Science* **275**, 1904–1907.

DEMYK K. (2000) Les silicates interstellaires: Composition physico–chimique et évolution. Ph.D. thesis, Université de Paris-XI, Paris, France.

DEMYK K., JONES A. P., DARTOIS E., COX P. AND D'HENDECOURT L. (1999) The chemical composition of silicate dust around RAFGL7009S and IRAS 19110+1045. *Astron. Astrophys.* **349**, 267–275.

DEMYK K., CARREZ P., LEROUX H., CORDIER P., JONES A. P., BORG J., QUIRICO E., RAYNAL P. I. AND D'HENDECOURT L. (2001) Structural and chemical alteration of crystalline olivine under low energy He^+ irradiation. *Astron. Astrophys.* **368**, L38–L41.

DORSCHNER J., FRIEDEMANN C., GUERTLER J. AND HENNING T. (1988) Optical properties of glassy bronzite and the interstellar silicate bands. *Astron. Astrophys.* **198**, 223–232.

DUKES C. A., BARAGIOLA R. A. AND MCFADDEN L. A. (1999) Surface modification of olivine by H^+ and He^+ bombardment. *J. Geophys. Res.* **104**, 1865–1872.

EBY R. K., EWING R. C. AND BIRTCHER R. C. (1996) The amorphization of complex silicates by ion-beam irradiation. *J. Mater. Res.* **7**, 3080–3102.

FABIAN D., JÄGER C., HENNING TH., DORSCHNER J. AND MUTSCHKE H. (2000) Steps toward interstellar mineralogy. V. Thermal evolution of amorphous magnesium silicates and silica. *Astron. Astrophys.* **364**, 282–292.

HALLENBECK S. L., NUTH J. A. AND DAUKANTAS P. L. (1998) Mid-infrared spectral evolution of amorphous magnesium silicate smokes annealed in vaccum: Comparison to cometary spectra. *Icarus* **131**, 198–209.

HARKER D. E., WOODEN D. H., WOODWARD C. E. AND LISSE C. M. (2002) Grain properties of comet C/1995 O1 (Hale Bopp). *Astrophys. J.* (in press).

JOHNSON P. B., GILBERD P. W., MARKWITZ A., RAUDSEPP A. AND BROWN I. W. M. (2000) Helium ion implantation in SiAlON: Characterization of cavity structures using TEM and IBA. *Nucl. Instrum. Methods B* **166–167**, 121–127.

JONES A. P. (2000) Depletion patterns and dust evolution in the interstellar medium. *J. Geophys. Res.* **105**, 10 257–10 268.

JONES A. P., TIELENS A. G. G. M. AND HOLLENBACH D. J. (1996) Grain shattering in shocks: The interstellar grain size distribution. *Astrophys. J.* **469**, 740–764.

KELLER L. P. AND MCKAY D. S. (1997) The nature and origin of rims on lunar soil grains. *Geochim. Cosmochim. Acta* **61**, 2331–2341.

KEMPER F., DE KOTER A., WATERS L. B. F. M., BOUWMAN J. AND TIELENS A. G. G. M. (2002) Dust and the spectral energy distribution of the OH/IR star OH 127.8+0.0:line. Evidence for circumstellar metallic iron. *Astron. Astrophys.* **384**, 585–593.

KESSLER M. F. *ET AL.* (1996) The Infrared Space Observatory (ISO) mission. *Astron. Astrophys.* **315**, L27–L31.

LI A. AND DRAINE B. T. (2001) On ultrasmall silicate grains in the diffuse interstellar medium. *Astrophys. J.* **550**, L213–L217.

MALFAIT K., WAELKENS C., WATERS L. B. F. M., VANDENBUSSCHE B., HUYGEN E. AND DEGRAAUW M. S. (1998) The spectrum of the young star HD 100546 observed with the Infrared Space Observatory. *Astron. Astrophys.* **332**, L25–L28.

MASCHHOFF B. L. AND ARMSTRONG N. R. (1991) Thin oxide layers on clean surfaces: Formation under vacuum and characterization by photoelectron spectroscopy and electrochemical reactions of probe molecules at the oxide/electrolyte interface. *Langmuir* **7**, 693–703.

MESSENGER S. (2000) Identification of molecular-cloud material in interplanetary dust particles. *Nature* **404**, 968–971.

MOLSTER F. J., WATERS L. B. F. M., TILENS A. G. G. M., KOIKE C. AND CHIHARA H. (2002) Crystalline silicate dust around evolved stars. III. A correlations study of crystalline silicate features. *Astron. Astrophys.* **382**, 241–255.

RAINERI V., SAGGIO M. AND RIMINI E. (2000) Voids in silicon by He implantation: From basic to applications. *J. Mater. Res.* **15**, 1449–1477.

SASAJIMA N., MATSUI T., FURUNO S., HOJOU K. AND OTSU H. (1999) Damage accumulation in Al_2O_3 during H_2^+ or He^+ ion irradiation. *Nucl. Instrum. Methods B* **148**, 745–751.

SCOFIELD J. H. (1976) Hartree–Slater subshell photoionization cross-sections at 1254 and 1487 eV. *J. Electron Spectrosc. Relat. Phenom.* **8**, 129–137.

SHIRLEY D. A. (1972) High-resolution x-ray photoemission spectrum of the valence bands of gold. *Phys. Rev.* **5**, 4709–4714.

SMENTKOWSKI V. S. (2000) Trends in sputtering. *Progr. Surf. Sci.* **64**, 1–58.

SNOW T. P. AND WITT A. N. (1996) Interstellar depletions updates: Where all the atoms went. *Astrophys. J.* **468**, L65–L68.

TAMUNA S., POWELL C. J. AND PENN D. R. (1993) Calculations of electron inelastic mean free paths (IMFPs) IV. Evaluation of calculated IMFPs and the predictive IMFP formula TPP-2 for electron energies between 50 and 2000 eV. *Surf. Interface Anal.* **20**, 77–89.

TIELENS A. G. G. M. (1990) Towards a circumstellar silicate mineralogy. In *From Miras to Planetary Nebulae: Which Path for Stellar Evolution?* (eds. M. O. Mennessier and A. Omont), pp. 186–200. Proc. International Colloquium, Editions Frontieres, Gif-sur-Yvette, France.

VAN CAPPELLEN E. (1990) The parameterless correction method in x-ray microanalysis. *Microsc. Microanal. Microstruct.* **1**, 1–22.

VAN CAPPELLEN E. AND DOUKHAN J. C. (1994) Quantitative transmission x-ray microanalysis of ionic compounds. *Ultramicroscopy* **53**, 343–349.

WAELKENS C. *ET AL.* (1996) SWS observations of young main-sequence stars with dusty circumstellar disks. *Astron. Astrophys.* **315**, L245–L248.

WAELKENS C., MALFAIT K. AND WATERS L. B. F. M. (1998) ISO observations of isolated Ae/Be stars. *Astrophys. Space Sci.* **255**, 25–33.

WAGNER C. D., DAVIS L. E. AND RIGGS W. M. (1980) The energy dependence of the electron mean free path. *Surf. Interface Anal.* **2**, 53–55.

WANG L. M., MILLER M. L. AND EWING R. C. (1993) HRTEM study of displacement cascade damage in krypton-ion-irradiated silicate–olivine. *Ultramicroscopy* **51**, 339–347.

WANG L. M., GONG S. X., WANG S. X. AND EWING R. C. (1999) Comparison of ion-beam irradiation effects in X_2YO_4 compounds. *J. Am. Ceram. Soc.* **82**, 3321–3329.

WANG S. X., WANG L. M. AND EWING R. C. (2000) Electron and ion irradiation of zeolites. *J. Nucl. Mater.* **278**, 233–241.

WATERS L. B. F. M. *ET AL.* (1996) Mineralogy of oxygen-rich dust shells. *Astron. Astrophys.* **315**, L361–L364.

WEBER W. J. *ET AL.* (1998) Radiation effects in crystalline ceramics for immobilization of high-level nuclear waste and plutonium. *J. Mater. Res.* **13**, 1434–1484.

WOODEN D. H. (2002) Comet grains: Their IR emission and their relation to interstellar medium grains. *Earth, Moon, Planets* (in press).

WOODEN D. H., HARKER D. E., WOODWARD C. E., BUTNER H. M., KOIKE C., WITTEBORN F. C. AND MCMURTRY C. W. (1999) Silicate mineralogy of the dust in the inner coma of comet C/1995 01 (Hale Bopp) pre-and post-perihelion. *Astrophys. J.* **517**, 1034–1058.

WOODEN D. H., BUTNER H. M., HARKER D. E. AND WOODWARD C. E. (2000) Mg-rich silicate crystals in comet Hale-Bopp: ISM relics or solar nebula condensates? *Icarus* **143**, 126–137.

ZIEGLER J. F., BIERSACK J. P. AND LITTMARK U. (1996) *The Stopping and Range of Ions in Solids.* Pergamon Press, New York, New York, USA. 321 pp.

APPENDIX

The appendix appears on the following page.

APPENDIX

In this section we describe the experimental and data processing methods used to obtain quantitative composition profiles on irradiated samples recorded by analytical TEM. Two major issues are addressed: (1) irradiated samples are unstable and might evolve under the electron probe during the analysis; (2) quantitative analysis in the TEM requires to determine the exact thickness of the specimen under the electron probe.

(1) The first issue has been addressed by chronospectroscopy. Three spectra have been recorded successively (*i.e.*, after 20, 40, 60 s) at each point, in order to detect a possible composition evolution under electron probe. In EDS microanalysis, the detected signal is a net count N or intensity I for each element detected. The concentrations C are deduced with respect to the concentration of a reference element, Si in our case. Using $k_{X/Si}$ factor (characteristic of the EDS system) and the k_{abs} absorption correction, C_X is deduced from the following relation (Van Cappellen, 1990).

$$C_X/C_{Si} = k_{X/Si} \times k_{abs} \times (I_X/I_{Si})$$

I_X and I_{Si} are the x-ray peak intensities of X and Si after background subtraction. For the thickness determination (for computing k_{abs}), the three spectra have been processed based on the Van Cappellen and Doukhan method (1994) for oxide compounds. By this method, thickness is deduced by comparing the intensity of O with those of the different cations. The sample thickness is adjusted until electroneutrality is reached in the quantification program. This processing yields a value for the thickness, which we call T_{calc} (which is approximately the same for the three spectra) and three compositions. In case of a drift of the composition during spectra acquisition, the initial true composition can be extrapolated at $t = 0$ s. There is a potential problem however with this data processing because the Van Cappellen and Doukhan method is based on the assumption that the sample is stoichiometric, which is not verified with irradiated samples. The calculated thickness T_{calc} is then overestimated due to the oxygen loss (as is the case for analyses coming from the thinnest areas).

(2) To resolve the above problem, we have for each spectra calculated the total number of detected counts N. This parameter is directly proportional to the thickness of the analysed volume. Plotting N *vs.* T_{calc} (Fig. 17) clearly shows the deviation from stoichiometric compositions for very thin regions. This plot allows however to determine the thickness profile of the specimen in the investigated area. Indeed, in thick regions, deviation from stoichiometry is negligible (because the thickness of the amorphized or damaged layer is small compared to the sample thickness and its own composition is not far from an olivine). The upper bound of the data points is thus constituted of measurements that are not affected by stoichiometry deviations. The true thickness profile (T_{true}) is obtained; it is shown by the straight line in Fig. 17. This value T_{true} is used to re-process the three spectra recorded at each point. The three resulting compositions are then extrapolated to zero acquisition time to obtain the true composition at this point.

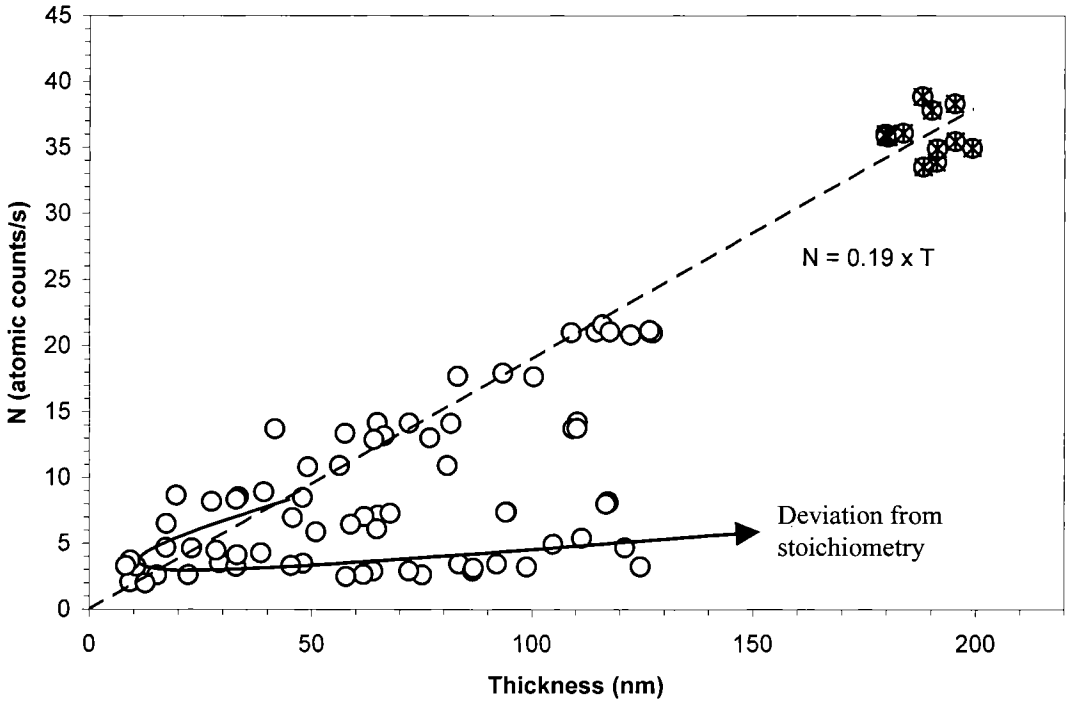


FIG. 17. Total x-ray counts are plotted against sample thickness. Only the thicker values (marked with a cross) are used to fit the relation between x-ray counts and thickness (see details in appendix). For low counts number, thickness is deduced from the linear fit.